Accepted Manuscript

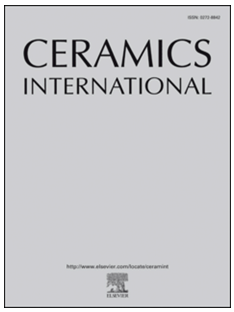

Silver-modified MoS_2 nanosheets as a high-efficiency visible-light photocatalysts for water splitting

Meiqin Li, Zhen Cui, Enling Li

PII: S0272-8842(19)30991-5

DOI: https://doi.org/10.1016/j.ceramint.2019.04.166

Reference: CERI 21360

To appear in: *Ceramics International*

Received Date: 3 April 2019

Revised Date: 18 April 2019

Accepted Date: 19 April 2019

Please cite this article as: M. Li, Z. Cui, E. Li, Silver-modified MoS_2 nanosheets as a high-efficiency visible-light photocatalysts for water splitting, *Ceramics International* (2019), doi: https://doi.org/10.1016/j.ceramint.2019.04.166.

Silver-modified MoS_2 nanosheets as a high-efficiency visible-light photocatalysts for water splitting

Meiqin Li,[a†] Zhen Cui*[a b†] and Enling Li*[a]

[a]*School of Science, Xi'an University of Technology, Xi'an 710048, P.R. China*

[b] *School of Automation and Information Engineering, Xi'an University of Technology, Xi'an 710048, P.R. China*

Abstract

One of the major challenges that the human beings are facing is the shortage of the fossil fuels. Hydrogen is considered as the most attractive renewable energy because of its abundant high energy density. Semiconductor photocatalytic technology for water decomposition is a promising method for converting sunlight into hydrogen energy, which has attracted considerable attention. Compared with bulk materials, two-dimensional (2D) materials exhibit remarkable photocatalytic properties. In this work, the pristine high-quality hexagonal molybdenum disulfide (MoS_2) nanosheets and Ag-doped MoS_2 nanosheets were synthesized by hydrothermal method, and the thickness of nanosheets was ranged from 0.9 to 1.1 nm. In addition, the absorption spectra of Ag-doped MoS_2 nanosheets increased with the increase of Ag content. What's more, the photocatalytic properties of Ag-doped MoS_2 nanosheets were tested, and the results show that Ag-doped MoS_2 nanosheets have good stability, high hydrogen production efficiency and strong photocatalytic activity. It is worth mentioning that the photocatalytic hydrogen production rate of Ag-doped MoS_2 nanosheets can reach 2695 umol h^{-1} g^{-1}. Meanwhile, density functional theory was used to calculate the optical properties, electronic structure of pristine and Ag-doped monolayer MoS_2. These calculated results indicate that the absorption intensity of Ag-doped MoS_2 in the ultraviolet-visible and visible light region increases significantly, and the conduction band of Ag-doped monolayer MoS_2 is downshift compared with pristine MoS_2. Therefore, Ag-doped MoS_2 can optimize the band

structure and promote the absorption of visible light, thereby improving the photocatalytic activity.

Keywords: Ag-doped MoS_2 nanosheets; Photocatalysis; Hydrothermal method; First principles;

* Corresponding author:E-mail:zcui@xaut.edu.cn; lienling@xaut.edu.cn

†:these authors contributed equally to this study.

1 Introduction

Hydrogen is a new energy source that is clean, environmentally friendly and efficient. Although hydrogen prepared by electrolytic water method is highly purified, environmentally friendly and renewable, the slow kinetic process of electrocatalytic hydrogen production greatly limits its energy conversion efficiency [1-6]. The disadvantage of high energy consumption of hydrogen is that noble metal catalysts (such as Pt/Pd) are usually needed to reduce the overpotential of electrocatalytic reaction. However, the high cost and scarcity of these catalysts greatly limit their industrial application.

Since the discovery in 1970s that water can be decomposed by using titanium dioxide (TiO_2) electrodes under ultraviolet radiation to produce hydrogen, and semiconductor materials have been rapidly developed in the field of photocatalytic decomposition of water [7-10]. In recent years, 2D nanomaterials have attracted much attention and have been researched in many fields due to their special optical and electrical properties. This studies show that the edges of 2D layered nanocrystals catalytic materials have the characteristics of few atomic sites and unsaturated coordination. They are easy to become active centers of catalysis. They have good catalytic activities in the fields of catalytic desulfurization, oxygen reduction and photocatalytic hydrogen production. Among various reported catalysts of 2D nanomaterials, 2D transition metal dichalcogenides (TMDs) are attracting more and

more researchers to study them. Compared with precious metals, TMDs have attracted much attention due to their excellent catalytic activity and low cost.

MoS_2, as a typical TMDs, has good catalytic hydrogen evolution performance, resulting scientists' great attention. Compared with the common bulk MoS_2, the nano-sized MoS_2 has superior performance, mainly showing a larger specific surface area, stronger adsorption capacity and higher reactivity. There are many factors that affect the catalytic activity of MoS_2. These factors include the number of layers of MoS_2, the dispersion and the number of active sites at different positions. Therefore, when the size of MoS_2 sheet is reduced to the nanometer scale, the ratio of the active sites would increase, and the catalytic efficiency can be remarkably improved. In order to improve the catalytic activity and energy conversion efficiency of MoS_2, it can be combined with other materials in order to obtain excellent catalytic effects. A large number of studies have shown that although the monolayer MoS_2 photolytic water catalyst has good theoretical catalytic efficiency and light absorption performance, it is still difficult to obtain ideal hydrogen conversion rate, partly because it is easy to hard agglomerate during preparation, making it difficult to fully exert its performance. Increasing the efficiency of MoS_2 photocatalytic solar hydrogen production by doping, binary and multiple synergies has been a research hotpot in recent years.

Since Karunadasa et al [11] found that MoS_2 can be photohydrolyzed to produce hydrogen, various MoS_2 nanophotocatalysts have been developed one after another. In order to improve its photohydrolysis performance, MoS_2 has been compounded with various functional nanomaterials (such as semiconductors, metals, carbon materials, metal oxides, etc.). Yin et al discovered that MoS_2 was chemically loaded on CdS. The photocatalytic activity of H_2 can be significantly improved by loading MoS_2 as a catalyst promoter, and the photocatalytic hydrogen production performance in lactic acid solution even exceeds the precious metal promoter such as Pt loaded on CdS [12]. Xiang et al reported a MoS_2/graphene-TiO_2 composite. It was found that the new composite exhibited a high photocatalytic hydrogen production rate (0.16

mmol h^{-1}), while MoS_2/graphene-CdS composite exhibited a hydrogen production rate of 2.0 mmol h^{-1} in lactic acid system[13-14]. Guo et al synthesized MoS_2 nanosheets with different layers, and they systematically studied the position of valence band, conduction band and even band gap of MoS_2 and the relationship between the corresponding photocatalytic HER activity and the number of layers of MoS_2. It was found that the lower the number of layers of MoS_2, the stronger the photocatalytic hydrogen production activity [15]. Li and Fu et al successfully synthesized MoS_2/g-C_3N_4 binary compounds by two-step method, that is, firstly g-C_3N_4 powder was synthesized by combustion method, then, the MoS_2/g-C_3N_4 binary promoter was synthesized by hydrothermal method. The hydrogen production experiment of photolysis water showed that the binary compound had good photo-generated carrier separation efficiency. When the mass fraction of MoS_2 is 0.5%, the hydrogen evolution rate reaches 23.1 μmol h^{-1}, which is 11.3 times than that of pure g-C_3N_4 [16-17]. Wang et al reported that transition metal doping can also significantly improve the photohydrolysis performance of MoS_2 [18]. This shows that the combination of MoS_2 and other materials can greatly improve its photocatalytic hydrogen production characteristics. Recently, MoS_2 composites with some new carbon materials have attracted wide attention, mainly using second-phase carbon materials with good conductivity to accelerate carrier transport, such as graphene, carbon nanotubes, carbon fibers and so on.

As a typical 2D layered TMDs, the successful combination of MoS_2 and metal can provide more effective catalytic sites for photocatalytic decomposition of water, and promote electron transfer and further enhance photocatalytic decomposition of water. In this paper, we focus on the catalytic performance of a Ag-doped MoS_2 nanosheet and the hydrothermal method to prepare the MoS_2-based composite.

2. Experimental section

2.1 Chemicals

The chemicals used in this work were of analytical reagent grade. Sodium molybdate dihydrate ($Na_2MoO_4 \cdot 2H_2O$), thioacetamide (CH_3CSNH_2), tungstosilicic acid hydrate ($H_4[Si(W_3O_{10})_4] \cdot xH_2O$), silver nitrate ($AgNO_3$), deionized water and ethanol were purchased from Sinopharm.

2.2 Preparation of pristine and Ag-doped MoS_2 nanosheets

In a typical synthesis process, the first step was to add sodium molybdate and thioacetamide to deionized water in turn, and then stirring for 10~30 min to obtain solution A. The second step was to add silicotungstic acid to solution A, stirring for 10~30min to obtain solution B. The third step was to transfer solution B to Teflon-lined stainless steel autoclave with a total volume of 50 mL. Hydrothermal synthesis was carried out in a muffle furnace at 160-200 □ for 18-48 hours. The fourth step, after cooling down to room temperature, the obtained product was washed with deionized water and absolute ethanol, and it was filtered to obtain a precipitate, and the obtained precipitate was dried, and then the product obtained after drying was ground into powders to obtain MoS_2 nanosheets.

In the meantime, the formation process of Ag-doped MoS_2 nanosheets was introduced. Usually, silver nitrate is used as a silver source at a concentration of 0.1006 mol/L. In the first step, MoS_2 nanosheets obtained under the optimum process conditions were added to silver nitrate solution and transferred to Teflon-lined stainless steel autoclave with a total volume of 50 mL. In the steel autoclave, the hydrothermal reaction time was set to 48 h and the reaction temperature was 200 °C. In the second step, after the reaction was completed, the obtained product was washed several times with deionized water and absolute ethanol, and then it was filtered, and later the obtained precipitate was dried at 60 °C for 12 h, and the obtained black product was ground into powders, and the Ag-doped MoS_2 nanosheets photocatalyst were obtained. In the third step, Ag-doped MoS_2 nanosheets of different concentrations were prepared by controlling the ratio of silver nitrate.

2.3 Characterization of the materials

The products were characterized accordingly. The morphology of the samples was studied by scanning electron microscopy (SEM). The crystalline phases of the products were characterized by using X-ray diffraction (XRD). And X-ray photoelectron spectroscopy (XPS) was performed. TEM images were conducted on a JEM-3010 transmission electron microscope operated at 300 kV. High resolution transmission electron microscopy (HRTEM) images were carried out. The UV-visble diffuse reflectance spectra (DRS) were tested with a UV-visble spectrophotometer (UV-3101, Shimadzu).

2.4 Evaluation of photocatalytic performannce

In the experiment, pristine MoS_2 and Ag-doped MoS_2 nanomaterials were selected for research. The light source used in the room temperature environment was a 300W xenon lamp, equipped with an ultraviolet cut filter ($\lambda \geq 420$ nm) to eliminate ultraviolet light and water filter to remove infrared light, and the sacrificial agent was triethanolamine (TEOA), using 0.4 mM eosin Y as Sensitizer , and the catalyst was 50 mg, and the gas was detected by gas chromatography. The analyzer was equipped with a thermal conductivity detector (TCD) for gas chromatography (SP-6890, nitrogen as a carrier gas) to measure hydrogen. At the same time, we conducted three cycles of hydrogen production experiments to verify the stability of hydrogen production of the catalyst.

3. Results and discussion

The pristine MoS_2 and Ag-doped MoS_2 nanosheets composites were prepared by two-step hydrothermal process, and the morphology of the product was observed by SEM. As shown in Fig. 1, the pristine MoS_2 nanosheets and Ag-doped MoS_2 nanosheets have very smooth and uniform surfaces. The thickness of pristine MoS_2 nanosheets and Ag-doped MoS_2 nanosheets were ranged from 0.9 to1.1 nm. Fig. 1(a-b) are SEM images of the pristine MoS_2 nanosheets prepared by this work under optimal process conditions, which are high and low magnification images, respectively. Fig. 1(c-h) are SEM images of Ag-doped MoS_2 nanosheets with Ag content ratios of

1.95%, 4.27%, and 7.37%, respectively. It also can be seen from Fig. 1 that a large number of nanosheets are produced, and the nanosheets are thinner and smaller, and the layer-to-layer dispersion is good. The surface is smooth and the thickness is about 1 nm. This structure tends to possess a large specific surface area. The large specific surface area directly determines the existence of more active sites in the structure, which will undoubtedly show the advantages in photocatalytic experiments.

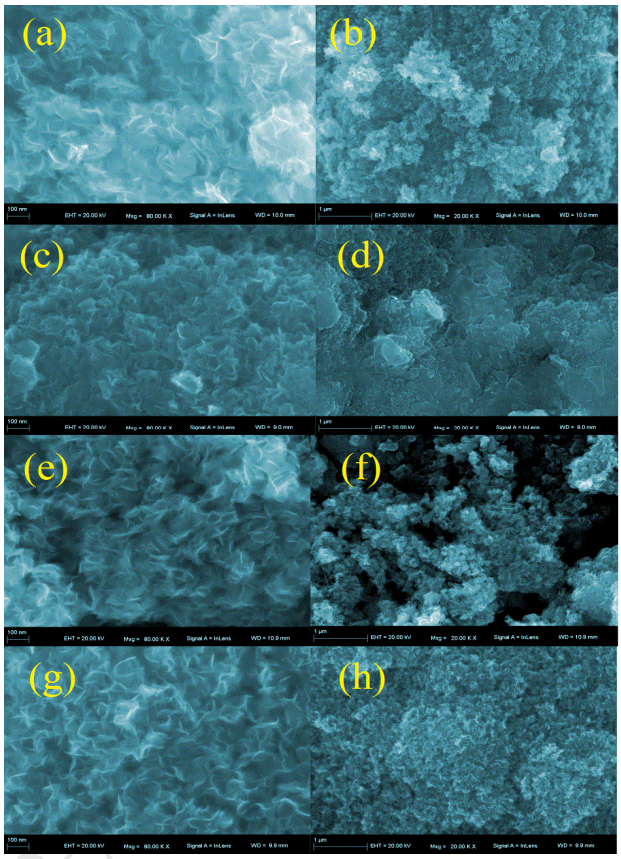

Fig. 1 (a-b) The SEM images of high and low magnification of pristine MoS_2 nanosheets. (c-d) SEM images of high and low magnification of Ag-doped MoS_2 nanosheets with Ag content of 1.95%. (e-f) The SEM images of high and low magnification of Ag-doped MoS_2 nanosheets with Ag content of 4.27%. (g-h) The SEM images of high and low magnification of Ag-doped MoS_2 nanosheets with Ag content of 7.37%.

Fig. 2 presents the corresponding energy dispersion spectra (EDS) of pristine MoS_2 nanosheets and Ag-doped MoS_2 nanosheets with Ag content ratios of 1.95%, 4.27%, and 7.37%, respectively. According to the test results shown in Fig. 2 (a), we

can see that the sample consists of elements of Mo and S, and no other elements have been observed. In addition, the quantification of the peak indicates that the atomic ratio between Mo and S is about 1:2.2, which is very close to stoichiometric MoS_2, so the product is undoubtedly MoS_2. From the test results of Fig. 2 (b-d), it can be seen that the products obtained have Ag element and no other impurity peaks, and the atomic number ratios of Mo to S of nanomaterials prepared with different Ag doping concentration are about 1:1.9, 1:1.7 and 1:1.8, which are basically close to the stoichiometric ratios of MoS_2. In addition, from the test results of Fig. 2 (b-d), it can be seen that the Ag content ratios are 1.95%, 4.27% and 7.37%, respectively.

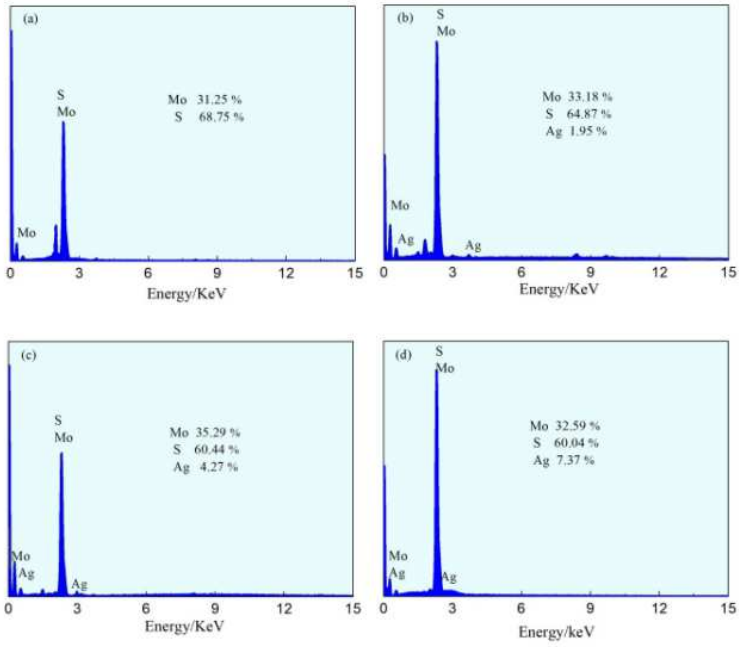

Fig. 2. (a) The EDS image of pristine MoS_2 nanosheets. (b) The EDS image of Ag-doped MoS_2 nanosheets with Ag content ratios of 1.95%.(c) The EDS image of Ag-doped MoS_2 nanosheets with Ag content ratios of 4.27%, (d) The EDS image of Ag-doped MoS_2 nanosheets with Ag content ratios of 7.37%.

In order to further identify the crystal structure of the prepared samples, XRD tests of different products were carried out. Fig. 3 is the XRD spectra of pristine MoS_2 nanosheets and Ag-doped MoS_2 nanosheets prepared by this work. The corresponding crystal planes at diffraction angle of 13.9, 33.3, 39.5 and 58.9 degrees are (002), (100),

(103) and (110) respectively. After comparison and analysis by professional software Jade, it is found that, (002), (100), (103), (110) diffraction peaks are consistent with those of classical 2H-MoS_2 standard cards (JCPDS cards (37-1492)). No additional peaks were observed in the XRD diagram, indicating the high purity of MoS_2 samples. Pristine MoS_2 nanomaterials with hexagonal system were prepared [19]. And Ag atoms have been doped into the prepared MoS_2 nanosheets.

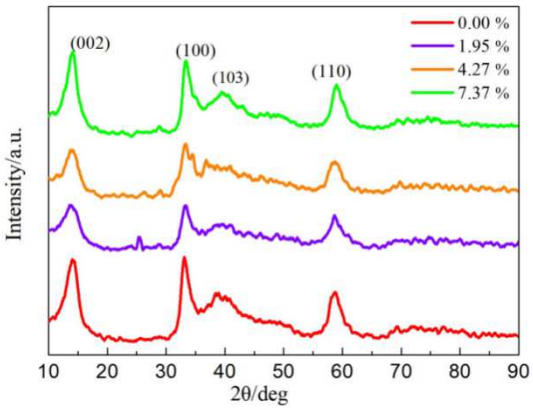

Fig. 3. The XRD image of pristine MoS_2 nanosheets and Ag-doped MoS_2 nanosheets with Ag content ratios of 1.95% and 4.27% and 7.37%, respectively.

XPS is used to further determine the elemental composition and elemental valence of the prepared samples, as is shown in Fig. 4. The 0~1200 eV full spectrum scanning results of the sample are shown in Fig. 4(a). The elements detected by full-spectrum scanning mainly include molybdenum, sulfur, oxygen, carbon and silver. It is mainly derived from carbon in the air. Its binding energy is around 288.0 eV, and the oxygen binding energy is generally around 531.0 eV. The main source of oxygen is from the air or the exposure of MoS_2 to air to form molybdenum trioxide. Oxygen, Mo 3d, S 2p and Ag 3d were subjected to peak separation treatment by the peak software. It can be seen from Fig. 4(b) that the photoelectron peak of molybdenum is composed of five peaks, and the binding energy is 231.9 eV and 231.1 eV, respectively, corresponding to molybdenum two peaks of Mo $3d_{5/2}$ and Mo $3d_{3/2}$ of (4^+) ions. It is mainly composed of molybdenum ions in molybdenum disulfide and molybdenum ions in a small amount of molybdenum dioxide, and the binding energy

is 233.3 eV, 234.6 eV and 236.6 eV, respectively, corresponding to Mo $3d_{5/2}$ and Mo $3d_{3/2}$ of molybdenum (6^{+}) ions. It is possible that the molybdenum dioxide introduced by the side reaction is exposed to molybdenum ions introduced by the oxidation of molybdenum trioxide in the air. From the above analysis, it can be inferred that the main compositions of the prepared MoS_2 nanosheets are MoS_2, a small amount of molybdenum dioxide and molybdenum trioxide. The binding energy of Fig. 4(c) is 378.4 eV and 372.4 eV, respectively, corresponding to two peaks of Ag $3d_{3/2}$ and Ag $3d_{5/2}$ of Ag (1^{+}) ions. The binding energy of Fig. 4(d) is 163.2 eV and 166.4 eV, corresponding to two peaks of S $2p_{3/2}$ and S $3p_{5/2}$ of sulfur (2^{-}) ions, respectively. It can be inferred from the above analysis that the prepared nanosheets are Ag-doped MoS_2 nanosheets.

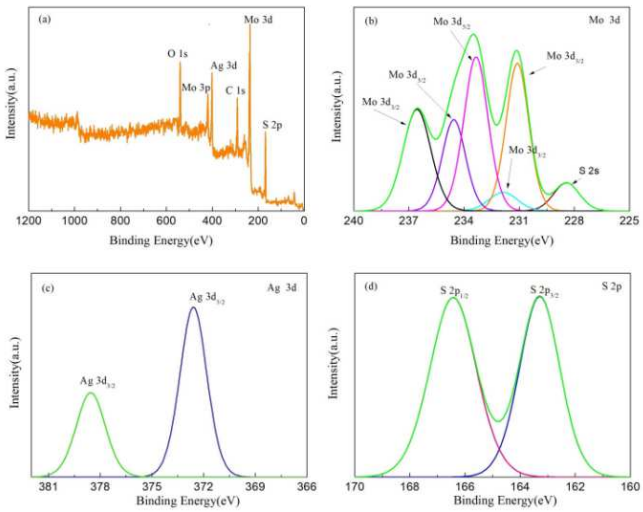

Fig. 4. The X-ray photoelectron spectroscopy (XPS) image of an Ag-doped MoS_2 nanosheet with an Ag content of 7.37%. (a) The Ag-doped MoS_2 nanosheet XPS master. (b) The XPS spectrum of the Mo 3d element. (c) The XPS map of Ag 3d elements. (d) The XPS map of S 2p elements.

The typical TEM images and HRTEM image of Ag-doped MoS_2 nanosheets with doping concentration of 7.37% are shown in Fig. 5. As they are exhibited in the images of Fig. 5(a-c), under the preferred preparation conditions, the prepared Ag-doped MoS_2 nanosheets have the characteristics of nanosheet curvature, layer spacing, lack of position and interlayer misalignment, relatively good length and

structural order, and the length of the sheet is between 20 and 60 nm. What's more, we can see from Fig. 5 (d) that the lattice spacing of the neatly arranged regions is 0.66 nm, corresponding to the (002) crystal plane of 2H type MoS_2 (JCPDS 75-1539) [20]. The crystallinity of the sample was in agreement with the XRD results.

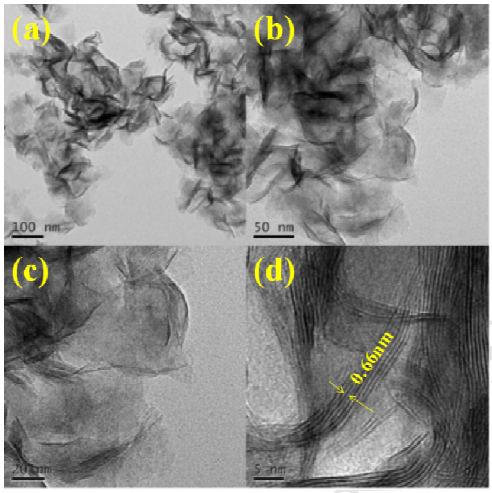

Fig. 5. (a-c) The TEM image of an Ag-doped MoS_2 nanosheets with an Ag content ratio of 7.37%. (d) The HRTEM image of an Ag-doped MoS_2 nanosheets with an Ag content ratio of 7.37%.

The structure of Ag-doped MoS_2 nanosheets with doping concentration of 7.37% composites is further studied by the EDS-mapping map. The results are shown in Fig.6. The distribution of S, Mo and Ag elements in the selected region can be clearly seen. And the samples are in full contact with different components. Similarly, the element distribution also shows that there is a high degree of hybridization between them, which can provide more catalytic sites.

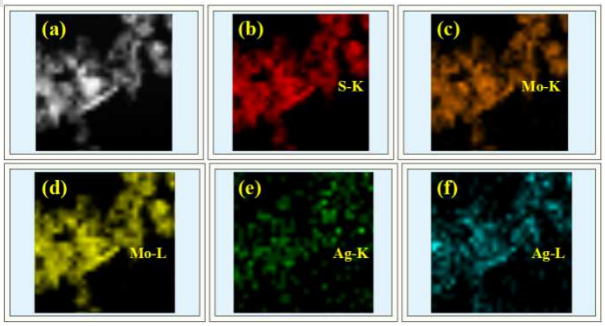

Fig. 6. EDS-mapping spectrum of element distribution of Ag-doped MoS_2 nanosheets with Ag content ratio of 7.37%.

Fig. 7 exhibits the UV-visible absorption spectra of the pristine MoS_2 nanosheets and Ag-doped MoS_2 nanosheets. The strong absorption of pristine and Ag-doped MoS_2 nanosheets in the near-ultraviolet region (from 200 to 450 nm) is attributed to the high UV absorption of MoS_2 nanosheets. At the same time, in the visible region (450-800 nm), the Ag-doped MoS_2 nanosheets composite shows more strong visble absorbance. For Ag-doped MoS_2 samples, the absorption wavelength of UV-visible spectra at 305 and 582 nm shows a slight blue shift compared with the pristine MoS_2 samples. In addition, with the increase of Ag content, the absorption of samples becomes stronger and stronger. This result confirmed that Ag-doped MoS_2 samples absorb both visible and ultraviolet light strongly, which indicates that Ag-doped MoS_2 composites have potential photodegradation of pollutants, such as Rhodamine B (RhB).

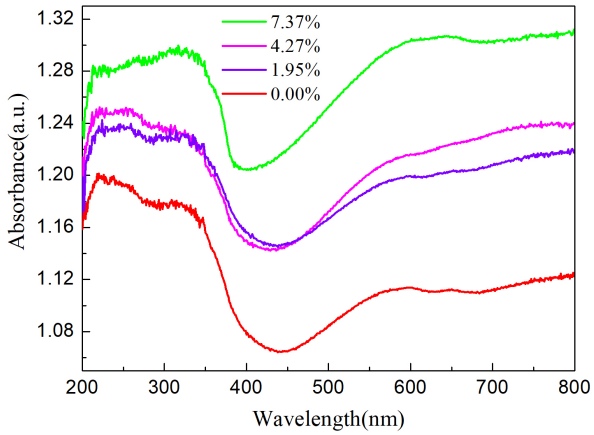

Fig. 7. The UV-visible absorption spectrum of pristine and Ag-doped MoS_2 nanosheets.

Fig. 8. shows the photocatalytic performance of the pristine and Ag-doped MoS_2 nanosheets with 7.37% doping concentration, which were in 15 ml TEOA aqueous solution (pH = 7) under visible light irradiation ($\lambda > 420$ nm). It can be seen from Fig. 8(a) that the pristine phase MoS_2 exhibits relatively weak photocatalytic activity, and the hydrogen production rate is 1708 μmol h^{-1} g^{-1}. It is worth noting that the photocatalytic hydrogen production rate of the prepared Ag-doped MoS_2 nanosheets can reach 2695 μmol h^{-1} g^{-1}. Furthermore, compared with noble metal catalysts,

MoS_2-based complexes have significant advantages as co-photocatalysts for H_2 production (Table 1). Therefore, the results tested indicate that the prepared Ag-doped MoS_2 nanosheets can significantly improve the photocatalytic hydrogen production efficiency. At the same time, as it is shown in Fig. 8. (b), in order to research the hydrogen production activity and stability of the Ag-doped MoS_2 catalyst, we performed three cycles for 18 hours, collecting 12 points every 6 hours, and passing 6 hours of light each time. Thereafter, the catalytic system was centrifuged and dried. After the catalyst was obtained, it was again dispersed in a new reaction solution for a new round of cycle experiments. With the increase of cycle times, the hydrogen production rate of the system remained at the same level, indicating that the catalytic activity of the composite photocatalyst did not change significantly. This shows that the catalyst has excellent stability.

Table 1. Summary of photocatalytic activity of MoS_2-based materials.

Samples	H_2 yield	References
p-MoS_2/*n*-rGO	160.6 μmol h^{-1} g^{-1}	[21]
0.5 wt.% MoS_2-g-C_3N_4	23.1 μmol h^{-1} g^{-1}	[22]
5 wt.% MSQD-CN	577 μmol h^{-1} g^{-1}	[23]
1.0 wt.% MoS_2/TiO_2	119.5 μmol h^{-1} g^{-1}	[24]
CdS-graphene-MoS_2	125 μmol h^{-1} g^{-1}	[25]
MoS_2/CdS	1800 μmol h^{-1} g^{-1}	[26]
TiO_2/MoS_2/graphene	165.3 μmol h^{-1} g^{-1}	[27]
MoS_2-NH_3	190 μmol h^{-1} g^{-1}	[28]
MoS_2-coated ZnO	1410 μmol h^{-1} g^{-1}	[29]
0.01 g CdSe/MoS_2	900 μmol h^{-1} g^{-1}	[30]
0.05 g MoS_2/CdS	3840 μmol h^{-1} g^{-1}	[31]
MoS_2 nanosheets	1708 μmol h^{-1} g^{-1}	this article
Ag-doped MoS_2 nanosheets	2695 μmol h^{-1} g^{-1}	this article

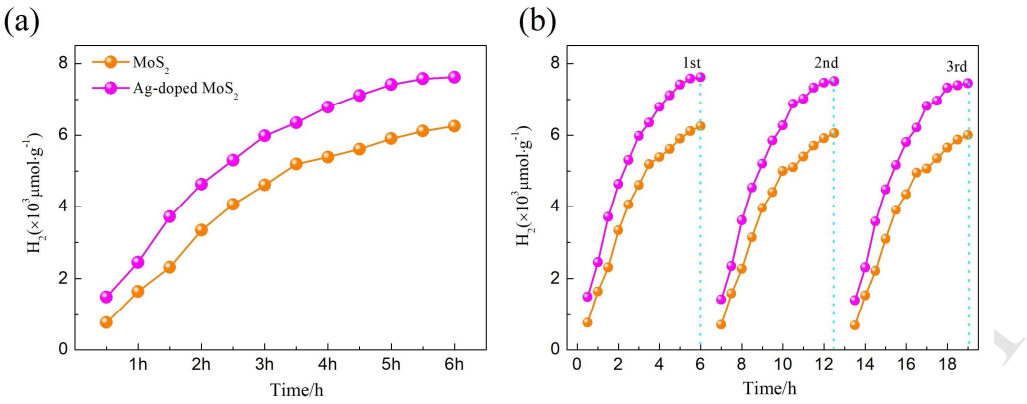

Fig. 8 (a) The hydrogen production effect diagram of pristine phase MoS_2 nanosheets and Ag-doped MoS_2 nanosheets with Ag content of 7.37%. (b) The cyclic catalytic hydrogen production effect test chart of pristine phase MoS_2 nanosheets and Ag-doped MoS_2 nanosheets with Ag content of 7.37%.

4. Theoretical simulation calculation section

The simulation has made a great contribution to the deep understanding and design of the new type of 2D photocatalyst. The theoretical study of 2D materials began in the early 1940s [32]. Many 2D materials, such as graphene [33-37], GaN [38-40], SnSe [41], silicon [42], and borophthalide [43], can be synthesized or observed experimentally only after theoretical prediction. In order to reveal the mechanism that the photocatalytic hydrogen production efficiency of Ag-doped MoS_2 is obviously improved, the optical properties and electronic structure of pristine and Ag-doped MoS_2 were investigated by density functional theory.

MoS_2 belongs to the hexagonal dense packing structure and consists of three atomic layers. The object of the calculation is a monolayer structure of MoS_2 crystals, in the doping system, and we replace the position of Mo with an Ag atom for substitutional doping of monolayer MoS_2, as exhibits in Fig. 9 (a). In addition, Fig. 9 (b) reveals the absorption coefficient for both pristine and Ag-doped MoS_2. Absorption coefficient a(ω) reflects the change in the transitions produced by the increase in energy after the material absorbs photons. From Fig. 9 (b), it can be seen that MoS_2 and Ag-doped MoS_2 have strong absorption in the near ultraviolet region

(from 150 to 400 nm), which is attributed to the high UV absorption of MoS_2. In addition, in the visible region (480-750 nm), the Ag-doped MoS_2 composite shows more strong visble absorbance. In short, after Ag doping, the absorption spectrum of MoS_2 becomes wider and the absorption intensity increases obviously. It can also be seen from Fig. 9. (b) that the absorption intensity of Ag-doped MoS_2 in the UV-visible region increases significantly. It is noteworthy that the simulation results are basically consistent with the experimental results. Meanwhile, in order to analyze the effect of Ag substitution doping on the electronic structure of monolayer MoS_2, the band structures of pristine MoS_2 and Ag-doped monolayer MoS_2 are calculated. As it is shown in Fig. 9 (c-d), the pink triangle represents the contribution of Mo atom, the blue diamond represents the contribution of S atom, and the green circle represents the contribution of Ag atom. From Fig. 9 (c) we can see that the pristine MoS_2 is a direct bandgap semiconductor with a bandgap of 1.68 eV, while the impurity band appears in the forbidden band of Ag-doped MoS_2 system as exhibited in Figure 9 (d). Compared with pristine MoS_2, the conduction band moves downward near the low energy region, while the valence band moves upward near the high energy region, and the bandgap width decreases to 0.76 eV. Therefore, Ag-doped MoS_2 can optimize the energy band structure to promote the absorption of visible light and the effective separation of photogenerated electron hole pairs, thereby improving the photocatalytic activity.

5. Photocatalytic hydrogen production mechanism

Fig. 10 exhibits a schematic diagram of the photocatalytic hydrogen production process. They include the absorption of light from semiconductor photocatalysts, the generation of electron carriers (electrons and holes), the recombination of electrons and holes, the migration of electrons and holes, and the trapping of charge carriers [44-45]. When we irradiate the catalyst with a beam of light of sufficient energy, the electrons in the valence band (VB) of the semiconductor photocatalyst absorb photons to the conduction band (CB), and holes are formed on the valence band, thus generating electron-hole pairs inside the semiconductor. After the electron-hole pair is

generated, the electron hole separation and recombination occurring inside the semiconductor are two important competitive processes, which greatly affect the efficiency of photocatalytic decomposition of water reaction [46]. If the electron-hole pairs are separated, the photogenerated electrons will be transferred to the cocatalyst and will undergo a reduction reaction with the water molecules to generate hydrogen gas. If electrons and holes recombine, the process will be divided into inactivation processes. Effective charge separation and rapid transfer of carriers avoid semiconductor internal/surface charge recombination, which is very important for photocatalysis to produce hydrogen by decomposing water. In this work, element doping modification is mainly to introduce metal ions into the semiconductor lattice, so that the semiconductor crystal generates defects or changes the lattice structure, after the introduction of Ag, the conduction band moved down, which promoted the generation of hydrogen and improved the photocatalytic activity of the band gap semiconductor.

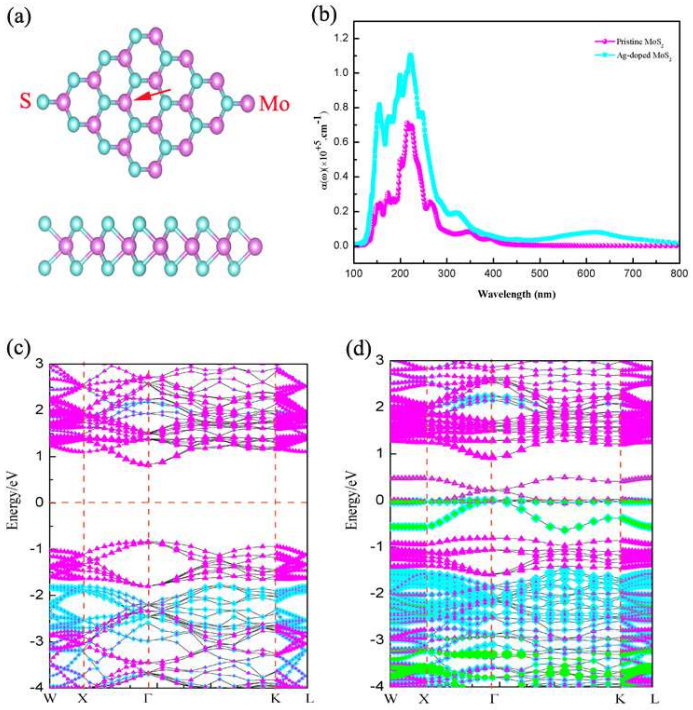

Fig. 9. (a) The top view and the side view model of pristine MoS_2 and Ag-doped MoS_2. (b) The absorption coefficient of pristine MoS_2 and Ag-doped MoS_2. (c) The energy band structure of pristine MoS_2 . (d) The energy band structure of Ag-doped MoS_2.

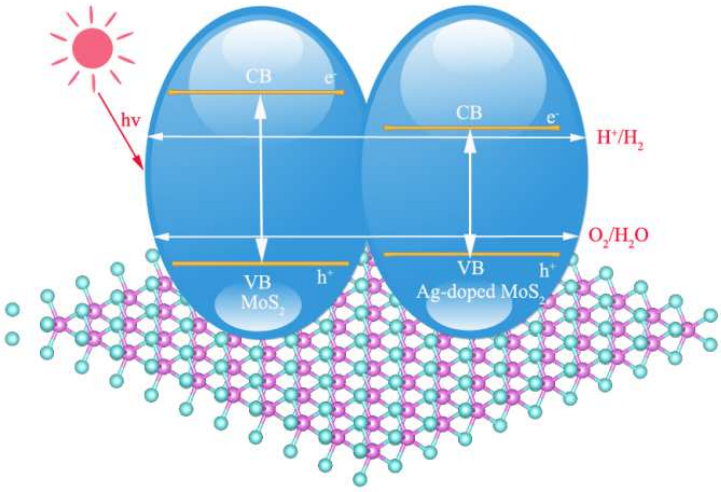

Fig. 10. The photocatalytic hydrogen production mechanism diagram

6. Conclusion

In this work, the pristine high-quality hexagonal structure MoS_2 and Ag-doped MoS_2 nanosheets were prepared by hydrothermal method. The as-prepared samples were carefully characterized by different characterization methods. Meanwhile, we used density functional theory to calculate the optical properties and electronic structure of pristine and Ag-doped MoS_2. The following conclusions can be drawn, (1) The thickness of pristine MoS_2 nanosheets and Ag-doped MoS_2 nanosheets was ranged from 0.9 to 1.1 nm. (2) The absorption spectra of Ag-doped MoS_2 nanosheets increased with the increase of Ag content, and the absorption intensity of Ag-doped MoS_2 in the ultraviolet-visible region increased significantly. (3) The Ag-doped MoS_2 nanosheets had excellent photocatalytic hydrogen production performance. (4) The impurity Ag element can optimize the energy band structure of pristine MoS_2, and make the conduction band moved down, and promote the absorption of visible light and the effective separation of photogenerated electron hole pairs, thereby improving photocatalytic activity.

Acknowledgements

This work was supported by the National Natural Science Foundation of China (No.11747032), Science and Technology Project of Xi'an (No.

201805037YD15CG21(30)), Special scientific research project of Shaanxi Provincial Education Department(No. 18JK0565), Natural Science Basic Research Plan in Shaanxi Province of China (Program No.2017JQ6065), Innovation Project of Key Industry Chain in Shaanxi Province(No. 2017ZDCXL-GY-06-01), the Project of key projects of research and development in Shaanxi Province (No. S2018-YF-ZDGY-0106). First-principles calculations were carried out on the Chen Qingyun's group clusters at the Southwest University of Science and Technology.

Notes and references

1 Y. Zhang, K. Shimoda, T. Ichikawa, and Y. Kojima. Activation of ammonia borane hybridized with alkaline−metal hydrides: a low-temperature and high-purity hydrogen generation material. J Phys Chem c, 114(34) (2010), 14662-14664.

2 J. Wang, Y. Li, Y. Zhang. Precious□metal□free nanocatalysts for highly efficient hydrogen production from hydrous hydrazine. Adv Funct Mater 24(45) (2014), 7073-7077.

3 T. Jingqi, C. Ningyan, L. Qian, X. Wei, and S. Xuping. Cobalt phosphide nanowires: efficient nanostructures for fluorescence sensing of biomolecules and photocatalytic evolution of dihydrogen from water under visible light. Angew Chem Int Edit, 54(18) (2015), 5493-5497.

4 J. Wang, Y. L. Qin, X. Liu, and X. B. Zhang. In situ synthesis of magnetically recyclable graphene-supported Pd@Co core–shell nanoparticles as efficient catalysts for hydrolytic dehydrogenation of ammonia borane. J Mater Chem, 22(25) (2012), 12468-12470.

5 J. M. Yan, X. B. Zhang, S. Han, H. Shioyama, and Q. Xu. Iron-nanoparticle-catalyzed hydrolytic dehydrogenation of ammonia borane for chemical hydrogen storage. Angew Chem Int Edit 47(12) (2008), 2287-2289.

6 J. Su, X. Zou, G. D. Li, Y. M. Jiang, Y. Cao, and J. S. Chen. Room-temperature spontaneous crystallization of porous amorphous titania into a high-surface-area anatase photocatalyst. Chem Commun, 49(74) (2013), 8217-8219.

7 A. Fujishima and K. Honda. Electrochemical photolysis of water at a semiconductor electrode. Nature, 238(5358) (1972), 37.

8 A J. Bard. Photoelectrochemistry and heterogeneous photo-catalysis at semiconductors. J. Photochem, 10(1) (1979), 59-75.

9 A. J, Bard. Photoelectrochemistry. Science, 207 (4427) (1980), 139-144.

10 X. Chen, S. Shen, L. Guo, and S.S. Mao. Semiconductor-based photocatalytic hydrogen generation. Chem Rev, 110(11) (2010), 6503-6570.

11 H. I. Karunadasa, E. Montalvo, Y. Sun, M. Majda, J. R. Long, and C. J. Chang. A molecular MoS_2 edge site mimic for catalytic hydrogen generation. Science, 335(6069) (2012), 698-702.

12 X. L. Yin, L. L. Li, W. J. Jiang, Y. Zhang, X. Zhang, L. J. Wan and J. S. Hu. MoS_2/CdS nanosheets-on-nanorod heterostructure for highly efficient photocatalytic H_2 generation under visible light irradiation. Acs Appl Mater Inter, 8(24) (2016), 15258-15266.

13 J. H. Yu, H. R. Lee, S. S. Hong, D. Kong, H. W. Lee, and H. Wang. Vertical heterostructure of two-dimensional MoS_2 and WSe_2 with vertically aligned layers. Nano Lett, 15(2) (2015), 1031-1035.

14 B. Višić, L. S. Panchakarla, and R. Tenne. Inorganic nanotubes and fullerene-like nanoparticles at the crossroads between solid-state chemistry and nanotechnology. J Am Chem Soc, 139(37) (2017), 12865-12878.

15 B. Guo, K. Yu, H. Li, H. Song, Y. Zhang, and X. Lei. Hollow structured micro/nano MoS_2 spheres for high electrocatalytic activity hydrogen evolution reaction. Acs Appl Mater Inter, 8(8) (2016), 5517-5525.

16 J. Li, E. Liu, Y. Ma, X. Hu, J. Wan, and S. Lin. Synthesis of MoS_2/g-C_3N_4 nanosheets as 2D heterojunction photocatalysts with enhanced visible light activity. Appl Surf Sci, 364(2016), 694-702.

17 F. Hui, C. Battaglia, C. Carraro, S. Nemsak, B. Ozdol, and J. S. Kang. Low-temperature and ultrafast synthesis of patternable few-layer transition metal dichacogenides with controllable stacking alignment by a microwave-assisted selenization process. Chem Mater, 28(4) (2016), 1147-1154.

18 H. Wang, C. Tsai, D. Kong, K. Chan, F. Abild-Pedersen, and J. K. Nørskov. Transition-metal doped edge sites in vertically aligned MoS_2 catalysts for enhanced hydrogen evolution. Nano Res 8(2) (2015), 566-575.

19 J. Xiao, J. Zhang, W. Liu, T. Huang, Y. Qu, H. Chen, and Z. Lin. Construction of rGO/Bi_2MoO_6 2D/2D nanocomposites for enhancement visible light-driven photocatalytic reduction of Cr (VI). Mater Res Express, 5(11) (2018), 115031.

20 X. Zhang, H. Tang, M. Q. Xue, C. S. Li. Facile synthesis and characterization of ultrathin MoS_2 nanosheets. Mater Lett, 130 (2014), 83-86.

21 F. Meng, J. Li, S. K. Cushing, M. Zhi, and N. N. Wu. Solar hydrogen generation by nanoscale p–n junction of p-type molybdenum disulfide/n-type nitrogen-doped reduced graphene oxide. J Am Chem Soc, 135(28) (2013), 10286-10289.

22 Y.Tian, L. Ge, K. Wang, and Y. Chai. Synthesis of novel MoS_2/g-C_3N_4 heterojunction photocatalysts with enhanced hydrogen evolution activity. Mater Charact, 87(2014), 70-73.

23 Y. Liu, H. Zhang, J. Ke, J. Zhang, W. Tian, X. Xu, and S. Wang. 0D (MoS_2)/2D (g-C_3N_4) heterojunctions in Z-scheme for enhanced photocatalytic and electrochemical hydrogen evolution. Appl Catal B-Environ 228(2018), 64-74.

24 L. Qian, Z. Pu, A. M. Asiri, A. H. Qusti, A. O. Al-Youbi, and X. Sun. One-step solvothermal synthesis of MoS_2/TiO_2 nanocomposites with enhanced photocatalytic H_2 production. J Nanopart Res, 15(11) (2013), 2057.

25 T. Jia, A. Kolpin, C. Ma, R. C. Chan, W. M. Kwok, and S. C. Tsang. A graphene dispersed CdS–MoS_2 nanocrystal ensemble for cooperative photocatalytic hydrogen production from water. Chem Commun, 50(10)(2014), 1185-1188.

26 X. Zong, H. Yan, G. Wu, G. Ma, F.Wen, L. Wang, and C. Li. Enhancement of photocatalytic H_2 evolution on CdS by loading MoS_2 as cocatalyst under visible light irradiation. J Am Chem Soc, 130(23) (2008), 7176-7177.

27 Q. Xiang, J. Yu, and M. Jaroniec. Synergetic effect of MoS_2 and graphene as cocatalysts for enhanced photocatalytic H_2 production activity of TiO_2 nanoparticles. J Am Chem Soc, 134(15) (2012), 6575-6578.

28 J. Shi, Y. Zhang, Y. Hu, X. Guan, Z. Zhou, and L. Guo. NH_3 - treated MoS_2 nanosheets as photocatalysts for enhanced H_2 evolution under visible-light irradiation. J. Alloy Compd, 688 (2016), 368-375.

29 S. Zhang, F. Tang, J. Liu, W. Che, H. Su, W. Liu, and S. Wei. MoS_2-coated ZnO nanocomposite as an active heterostructure photocatalyst for hydrogen evolution. Radlat PhysChem, 2017 137 (2017), 104-107.

30 F. A. Frame, F. E. Osterloh. CdSe-MoS_2: a quantum size-confined photocatalyst for hydrogen evolution from water under visible light. J Phys Chem C, 114(23) (2010),10628-10633.

31 Y. Liu, H. Yu, X. Quan, and S. Chen. Green synthesis of feather-shaped MoS_2/CdS photocatalyst for effective hydrogen production. Int J Photoenergy, 2013(2013) 247516–247521.

32 P. R. Wallace. The band theory of graphite. Phys. Rev, 1947, 71(9) (1947), 622-634.

33 V. O. Özçelik, and S. Ciraci. Size dependence in the stabilities and electronic properties of \alpha-graphyne and its BN analogue. J Phys Chem C, 117(117) (2013), 2175–2182.

34 G. Li, Y. Li, H. Liu, Y. Guo, Y. Li, and D. Zhu. Architecture of graphdiyne nanoscale films. Chem Commun, 46(19) (2010), 3256-3258.

35 D. Malko, C. Neiss, F. Viñes, and A. Görling. Competition for graphene: graphynes with direction-dependent dirac cones. Phys Rev Lett, 108(8) (2012), 086804.

36 M. S. Asl, Nayebi, B., & Shokouhimehr, M. TEM characterization of spark plasma sintered ZrB_2–SiC–graphene nanocomposite. Ceram Int , 44(13) (2018), 15269-15273.

37 A. Arshad, J. Iqbal, I. Ahmad, & M. Israr. Graphene/Fe_3O_4 nanocomposite: interplay between photo-Fenton type reaction, and carbon purity for the removal of methyl orange. Ceram Int , 44(3) (2018), 2643-2648.

38 Z. Y. Al Balushi, K. Wang, R. K. Ghosh, R. A. Vilá, S. M. Eichfeld, J. D. Caldwell, S. Subramanian, Two-dimensional gallium nitride realized via graphene encapsulation, Nat Mater. 15 (2016) 1166-1171.

39 Z. Cui, X. Ke, E. Li, T. Liu, Electronic and optical properties of titanium-doped GaN nanowires, Mater. Des. 96 (2016) 409-415.

40 Z. Cui, E. Li, X. Ke, T. Zhao, Y. Yang, Y. Ding & S. Xu, Adsorption of alkali-metal atoms on GaN nanowires photocathode, Appl Surf Sci. 423 (2017) 829-835.

41 Z. Cui, X. Wang, Y. Ding, M. Li, Exploration work function and optical properties of monolayer SnSe allotropes, Superlattice Microst. 114 (2018) 251-258.

42 K. Takeda, & K. Shiraishi. Theoretical possibility of stage corrugation in Si and Ge analogs of graphite. Phys Rev B, 50(20) (1994), 14916.

43 Z. A. Piazza, H. S. Hu, W. L. Li, Y. F. Zhao, J. Li, and L. S. Wang. Planar hexagonal B_{36} as a potential basis for extended single-atom layer boron sheets. Nat Commun, 5(1) (2014), 3113.

44 K. Maeda, and Kazuhiko. Photocatalytic water splitting using semiconductor particles: history and recent developments. J Photoch Photobio C, 12(4) (2011), 237-268.

45 J. H.Carey, J. Lawrence, H.M. Tosine. Photodechlorination of PCB's in the presence of titanium dioxide in aqueous suspensions, B Environ Contam Tox, 16(6) (1976), 697-701.

46 A. L. Linsebigler, G. Lu, and J. T. Yates Jr. Photocatalysis on TiO_2 surfaces: principles, mechanisms, and selected results. Chem Rev, 95(3) (1995), 735-758.